AIAA SciTech Forum
6-10 January 2020, Orlando, FL
AIAA Scitech 2020 Forum

10.2514/6.2020-1058

Numerical Investigation of NASA Hump Using Co-flow Jet for Separation Control

Kewei Xu *, Yan Ren †, Gecheng Zha ‡
Dept. of Mechanical and Aerospace Engineering
University of Miami, Coral Gables, Florida 33124
E-mail: gzha@miami.edu

Abstract

This paper applies Co-flow Jet (CFJ) active flow control (AFC) on NASA hump and numerically studies its flow control performance to suppress flow separation at low energy expenditure. The effects of the CFJ injection and suction locations are studied. The experimental results of the baseline hump and the hump with steady blowing and suction are used to validate the accuracy of numerical method. The high fidelity in-house CFD code FASIP with the 2D Unsteady Reynolds averaged Navier-Stokes (URANS) equations with one-equation Spalart-Allmaras model is utilized. The validation is overall in very good agreement with the experiment for the baseline and steady blowing cases.

The numerical simulation indicates that using co-flow jet for the hump separation control is very effective and energy efficient. With injection location at 50%C and suction location at 70%C, a full flow attachment is achieved at C_μ=0.0077 with the CFJ power coefficient (P_c) of 0.0032 and the energy coefficient (C_E) of 0.0034. This is consistent with the previous observation for CFJ airfoil that placing the injection at the suction peak location minimizes the AFC energy cost. The present study also discovers that the optimum location for CFJ suction is at the location the hump surface slope reaches the minimum, which gives the lowest energy consumption. A study is also conducted to move the CFJ injection location downstream to the baseline flow separation onset position at 67%C and move the suction location into the adverse pressure gradient area. Such configuration significantly increases the energy consumption. The study indicates that applying the CFJ upstream of the flow separation with mixing under favorable pressure gradient is much more efficient than applying it at the baseline flow separation area under the adverse pressure gradient.

To further investigate the role of suction in the CFJ active flow control, the injection-only flow control is designed and numerically studied. Compared with the CFJ case, the minimum energy consumption for the injection only case with the separation removed is increased by 57% with C_E of 0.0055. For the injection only flow control, the injection location for the minimum energy consumption is not at the suction peak location of 50%C as for the CFJ, but at the onset of separation location of 67%C. These results indicate that the suction of the CFJ flow control is very beneficial for two reasons: 1) It energizes the boundary layer and makes the CFJ energy consumption significantly lower than the injection only flow control; 2) It provides the source of the mass flow for injection to make the CFJ self-contained zero-next-mass-flux flow control to avoid introducing mass flow from other source, which will incur extra energy consumption.

Nomenclature

AFC Active Flow Control

* Ph.D. Candidate
† Post-doctoral Researcher
‡ Professor, AIAA associate Fellow

AoA	Angle of attack
APG	Adverse pressure gradient
BC	Boundary condition
C	The hump length
C_E	Energy coefficient
C_μ	Jet momentum coef. $\dot{m}_j\, U_j/(q_\infty\, S)$
C_p	Constant pressure specific heat
CFJ	Co-flow jet
$FASIP$	Flow-Acoustics-Structure Interaction Package
H_t	Total enthalpy
$\dot{m}$	Mass flow
Ma	Mach number
P	CFJ Pumping power
P_c	Power coefficient $L/(q_\infty\, S\, V_\infty)$
PR	Total pressure ratio, Γ
P_t	Total pressure
R_e	Reynolds number
T_t	Total temperature
$URANS$	Unsteady-Reynolds-Averaged Navier-Stokes
U_j	Injection Jet velocity
V_∞	Freestream velocity
$ZNMF$	Zero-Net Mass Flux
α	Angle of attack
β	Sideslip angle
γ	Air specific heats ratio
δ	Deflection angle
Δz	Injection nozzle spacing
η	CFJ pumping system efficiency, propeller efficiency
ρ_∞	Freestream density
c	Subscript, stands for corrected
j	Subscript, stands for jet
t	Subscript, stands for total value

1 Introduction

Active Flow Control (AFC) has the potential to break through conventional aerodynamic limitations and provides significant performance improvement to aircraft systems, such as lift enhancement, drag reduction, separation suppression and noise mitigation. Various types of AFC have been developed in recent years. AFC is to add energy to the main flow in order to improve the performance of the flow system. Prandtl's rotating cylinder in 1934 was one of the earliest AFC [1]. However, systematic efforts to develop AFC techniques have only occurred recently.

The widely used AFC methods include the circulation control (CC) relying on jet injection and Coanda effect [2]. The CC flow control requires an external fluid source, which is often problematic from a systems perspective [3]. Synthetic jet [4, 5, 6, 7, 8] and plasma jet [9, 10, 11, 12, 13] are zero-net-mass-flux flow and require no external fluid sources. However, both the synthetic and plasma jets in general provide low input momentum due to low

energy conversion efficiency from electric to fluid power, typically 3% $\sim$ 10% [14, 15, 16] for synthetic jets and less than 1% for plasma actuators [17].

Recently, a zero-net-mass-flux co-flow jet(CFJ) AFC shows great promise to enhance airfoil performance by achieving ultra-high lift coefficient and high cruise efficiency at low energy expenditure [18, 19, 20, 21, 22, 23, 24]. As sketched in Fig. 1, a CFJ airfoil draws a small amount of mass flow into the airfoil near the trailing edge, pressurizes and energizes it using a micro-compressor embedded inside the airfoil, and then tangentially injects the same mass flow near the leading edge in the main flow direction.

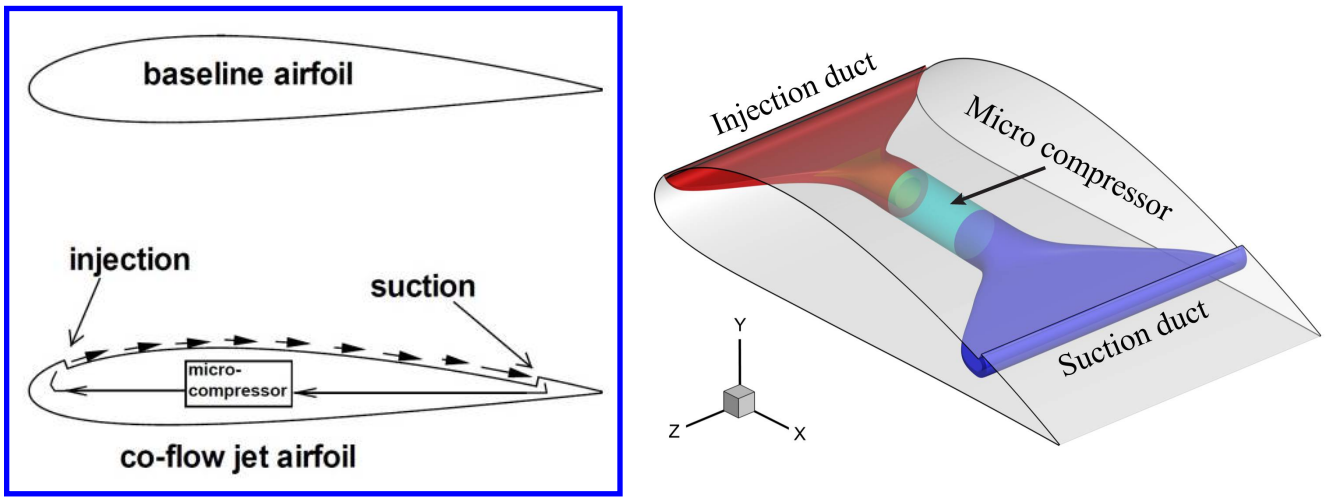

(a) 2D sketch (b) 3D sketch

Figure 1: Schematics of the CFJ airfoil

The fundamental mechanism of a CFJ airfoil is the turbulent mixing between the co-flow jet and the main flow, which energizes the boundary layer and allows the flow to overcome an extremely severe adverse pressure gradient (APG) and remain attached at a very large angles of attack. This results in an extraordinarily high lift coefficient [21, 22]. The CFJ airfoil has low energy expenditure because the jet is injected at the leading edge peak suction location where the local pressure is the lowest, hence requiring a low power to inject the flow. At the same time, the co-flow jet draws air near the trailing edge where the local pressure is nearly the highest, requiring a low power to suck in the flow. Furthermore, an important advantage of CFJ flow control is that the micro-compressor usually have very high energy conversion efficiency as turbomachinery, up to more than 80% [22, 25].

For a regular CFJ airfoil, the mixing process between the jet and main flow starts at the near lowest pressure location of the airfoil and ends at the near highest pressure location near trailing edge, as shown in Fig. 2 (a), which covers the major APG area. For a CFJ control surface of aircraft [26, 27, 28] as shown in Fig. 2 (b), the co-flow jet is not extended to the deflected flap area due to structure consideration. The APG area of a deflected control surface is mostly in the deflected flap area. A CFJ control surface hence has the major APG area uncovered by the coflow jet. However, a radical improvement of control surface lift coefficient (C_L) is still achieved with very high energy efficiency as indicated by the study of the authors' group in [26, 27, 28]. This encouraging result motivates this study to investigate effectiveness and efficiency of applying CFJ upstream of the APG area. The NASA hump with rapid diffusion and flow separation downstream of the throat is a very good candidate for this study.

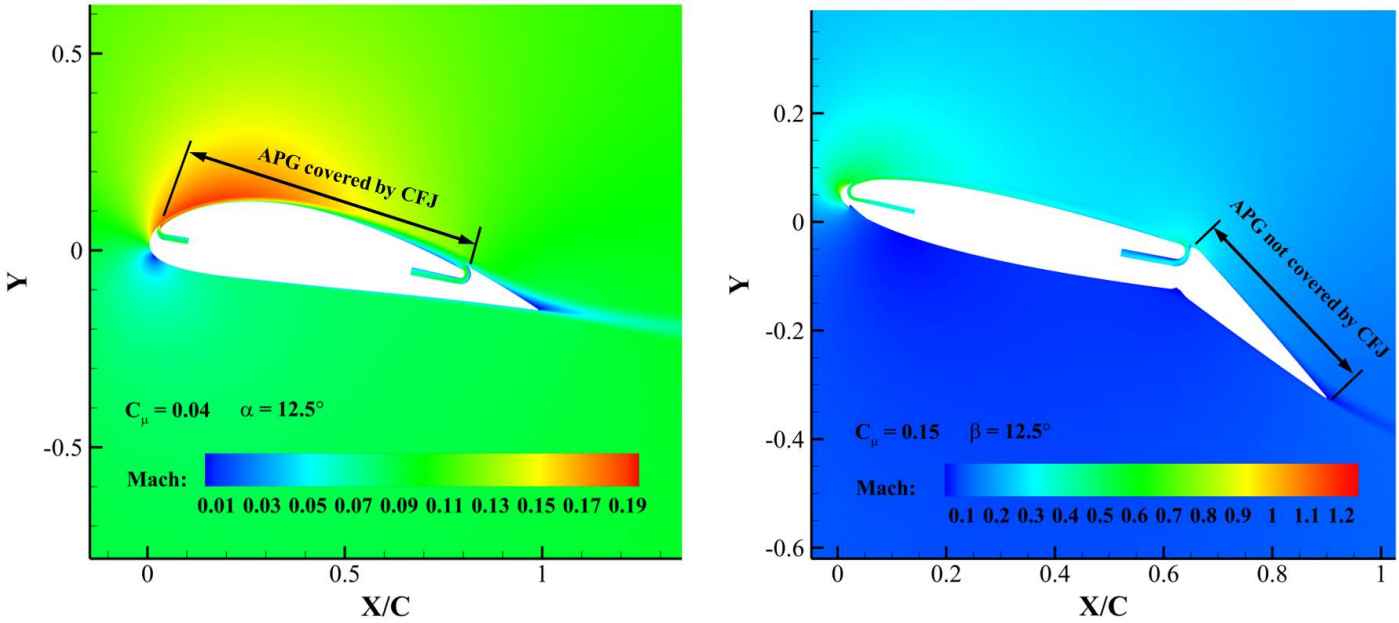

(a) Regular CFJ airfoil (b) CFJ control surface (adopted from [26])

Figure 2: Mach number contours of CFJ applications

1.1 The NASA Hump

The NASA hump is used as benchmark case to validate various numerical algorithms and turbulence modeling [29]. The baseline hump configuration with no flow control is designed to have a rapid area expansion downstream of the throat with a severe diffusion creating a massive flow separation [30], as shown in Fig. 3. The NASA hump flow separation control has practical significance for engine inlets or diffusers. For example, the serpentine inlets and boundary layer ingestion inlets are prone to flow separation that creates inlet flow distortion.

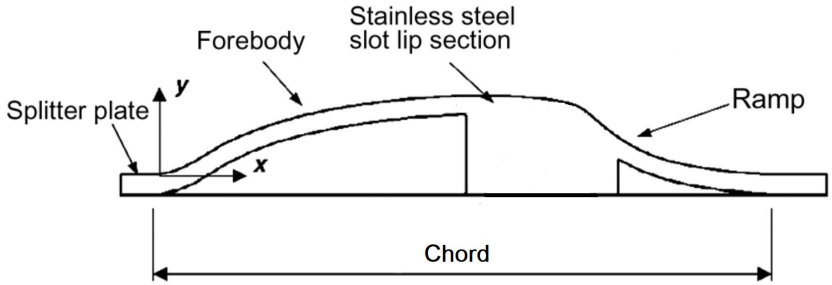

Figure 3: Geometry of hump upper surface [30]

The flow control methods studied to suppress the NASA hump flow separation include the injection only flow control [31] and suction only flow control [29]. For these two methods, the injection or suction is applied at the inception point of the flow separation of the baseline configuration. Applying certain jet injection or suction at the inception of the flow separation to suppress the separation is the typical practice in flow control. Such practice may be derived from the rationale that energizing the boundary layer right at the onset of the flow separation is

most effective and efficient.

Implementing injection only or suction only flow control in laboratory is straightforward. However, for the control volume covering the controlled flow such as an airfoil or a duct, the mass conservation is not satisfied. For example, for an injection only flow control, there must be a suction somewhere to provide the required mass flow for the injection. Where to withdraw the flow and how it affects the system efficiency are often not well addressed. Similarly, for the suction only case, where to dump the flow and their effect on the system is an important issue. For CFJ ZNMF flow control, the injection and suction are always together. However, where to place the injection and suction to have minimal energy expenditure is obliviously a very important question, which is one of the purposes of the present study.

2 CFJ Parameters

To facilitate the description of CFJ control surface performance, a few important parameters are given below.

2.1 Jet Momentum Coefficient

The injection jet momentum coefficient C_μ is used to describe the CFJ strength as:

$$C_\mu = \frac{\dot{m} V_j}{\frac{1}{2}\rho_\infty {V_\infty}^2 A_{ref}} \tag{1}$$

where $\dot{m}$ is the injection mass flow, V_j is the mass-averaged injection velocity, ρ_∞ and V_∞ denote the free stream density and velocity, and A_{ref} is the reference area defined as the product of chord length and hump span.

2.2 Power Coefficient

The CFJ power required is determined by the total enthalpy rise from the suction duct outlet to the injection duct inlet[20]. The total enthalpy rise can be achieved by the embedded micro-compressors or any pumping systems. The power required by the CFJ can be expressed as:

$$P = \frac{\dot{m} H_{t2}}{\eta}(\Gamma^{\frac{\gamma-1}{\gamma}} - 1) \tag{2}$$

where, $\dot{m}$ is the CFJ mass flow rate, H_{t2} is th total enthalpy at the suction slot, Γ is the total pressure ratio between the injection and suction, and η is the pumping system efficiency.

Eq. (2) indicates that the power required by the CFJ is linearly determined by the mass flow rate and exponentially by the total pressure ratio. This relationship in fact applies to all the active flow controls based on fluidic actuators including the injection only CC flow control. Thus, C_μ can not be used to represent the power consumption of active flow control [20, 32]. For example, a high C_μ could have a substantially lower power consumption than a smaller C_μ if the large C_μ is created by a high mass flow rate and low jet velocity, which only needs a significantly lower total pressure ratio [32, 33]. Yang and Zha [21] find that the only parameter correlated well with the maximum lift coefficient of CFJ airfoil is the power coefficient defined below:

$$P_c = \frac{P}{\frac{1}{2}\rho_\infty V_\infty^3 A_{ref}} \tag{3}$$

where P is the CFJ required power defined in Eq. (2).

3 CFD Simulation

3.1 CFD Code

The in-house high order CFD code Flow-Acoustics-Structure Interaction Package (FASIP) is used to conduct the numerical simulation. The 2D Unsteady-Reynolds averaged Navier-Stokes (URANS) equations with one-equation Spalart-Allmaras (SA) [34] turbulence model is used for this study. A 3rd order WENO scheme for the inviscid flux [35, 36, 37, 38, 39, 40] and a 4th order central differencing for the viscous terms [35, 39] are employed to discretize the Navier-Stokes equations. The low diffusion E-CUSP scheme used as the approximate Riemann solver suggested by Zha et al [36] is utilized with the WENO scheme to evaluate the inviscid fluxes. The second order time accurate implicit time marching method using Gauss-Seidel line relaxation is used to achieve a fast convergence rate [40]. Parallel computing is implemented to save wall clock simulation time [41, 42]. The FASIP code is intensively validated for CFJ simulations [43, 44, 45, 46, 47, 41, 48, 49, 50, 20, 51, 52]. All the simulations in this study are conducted as unsteady time accurate simulations. Since the experimental results reported are time averaged results, the numerical results are also presented as the time averaged results after 200 characteristic time when the flow and all the aerodynamic forces become dynamically stable.

3.2 Geometry and Boundary Conditions

The hump geometry shown in Fig. 3 has the upper surface of GlauertGoldschmied airfoil and the computational domain is created based on the experiment setup described in [30, 31].

The 2D computational domain is normalized by the hump chord of 420mm. A medium size mesh of 44,064 cells is used for baseline calculation as shown in Fig. 4. The boundary conditions (BCs) set-up is presented in Fig. 5. The inlet is located 6C upstream and the outlet is located 3C downstream of the hump. The total pressure, total temperature and flow angle are specified at the inlet as the boundary conditions. The static pressure is specified at the outlet boundary. Top wall is 0.9C away from the hump peak as designed in [31, 30]. Non-slip wall BC is applied on all the walls. The experimental conditions with inlet Mach number of 0.1 and the Reynolds number of 0.93×10^6 based on [30] are used for this study.

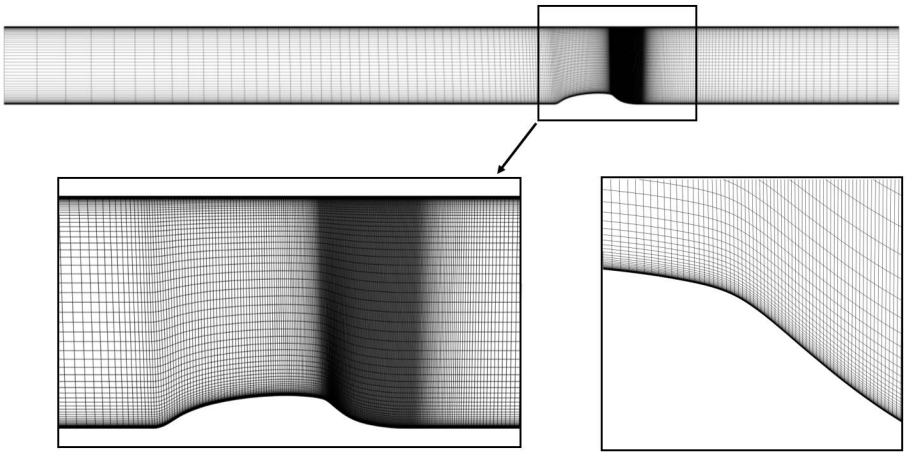

Figure 4: 2D computational mesh of baseline hump

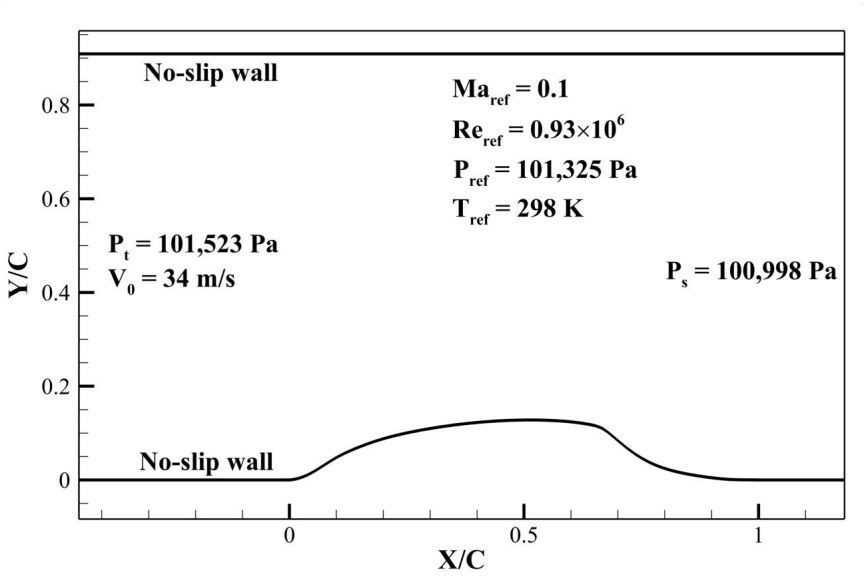

Figure 5: Boundary conditions of baseline hump simulation

Both the experimental steady injection and suction cases [29, 31] are used to validate the code. The configuration of the steady blowing jet created by Borgmann et al [31] is used in this study. The blowing actuator is located at X/C = 0.68 and angled at 10° to the freestream direction. For the suction only case, the hump geometry is the same as the injection only case with the injection slot replaced by a suction plenum located at X/C = 0.65 and the mesh is directly adopted from NASA resource [29].

The co-flow jet actuator is simulated with different injection location ranging from 15%C to 67%C and suction location ranging from 66%C to 90%C. The injection direction of co-flow jet is tangential to the local hump surface. This differs from the original flow controlled NASA hump whose injection is not tangential to the hump surface, but at an angle of 10° to the freestream direction. The other difference between the CFJ hump and the NASA hump is the slot size. The NASA hump has the injection slot size of 0.2%C. For the CFJ hump studied in this paper, two injection slot size of 0.5%C and 0.25%C are used.

3.3 CFD Validation

In the experiment, the model is tested in a open-return wind tunnel with freestream velocity of 34m/s (Mach = 0.1). The Reynolds number for all the cases is 0.93×10^6. The CFD simulations use the same experimental Mach number and Reynolds number. The CFD results of C_p distributions are validated with the experimental data provided in [30, 31]. Three cases are validated: the baseline hump, the hump with steady blowing, and the hump with steady suction. Mesh refinement studies are also conducted by doubling the number of grid points in i, j direction simultaneously, which produces the mesh size of 0.2 million cells.

Fig. 6 (a) presents the instantaneous Mach number contour of the baseline hump, which has a flow separation starting at X/C = 0.68 and reattaching at X/C = 1.15. The size of separation bubble and reattach location agree very well with the experiment measurement [29]. Based on the experiment, the static pressure at x/c=-2.5 is used as the reference pressure in C_p calculation for all the cases. Fig. 6 (b) is the predicted C_p distributions of the baseline hump compared with the experiment [30, 31]. Following the practice in [29, 53], the predicted time-averaged C_p distributions from simulation are shifted by -0.033 to better match the experimental upstream reference conditions. Fig. 6 (b), the simulated C_p distributions of the baseline hump agree very well with experimental measurement, except the pressure rise spike at the hump leading edge (X/C=0) is a little underestimated. The mesh refinement studies shown in Fig.6 (b) do not change the calculated results.

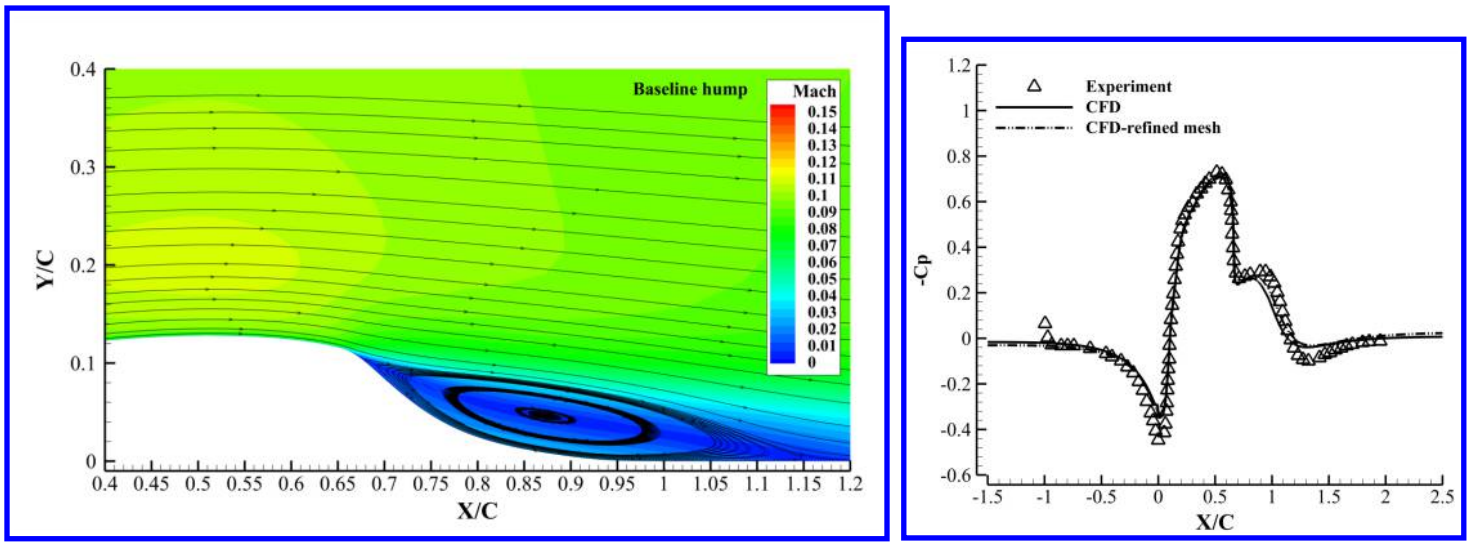

(a) Mach number contour of baseline hump (b) C_p distribution of baseline hump

Figure 6: CFD results of baseline hump

To further validate the numerical algorithms and CFD code, the hump cases with steady injection and suction were simulated and compared with the experimental data. Fig. 7 (a) is the Mach number contour of steady injection with C_μ=0.9% and U_j=85 m/s that are used in the experiment [31]. Steady blowing jet fully attaches the flow. The C_p distributions in Fig. 7 (b) shows that the predicted pressure distribution is again in very good agreement with the experiment [31]. The spike downstream of the suction peak is due to the jet injection. The solution is converged based on the mesh refinement.

The last simulation validation case is the one with steady suction of C_μ= 0.241% (mass flow coefficient C_Q= 0.15% [54]). The Mach number contours in Fig. 8 indicates that the suction only flow control is not adequate to remove the flow separation. The predicted C_p distributions with mesh refinement are shown in Fig. 8. The

CFD results are in good agreement with the experiment [29], but with the pressure rise under-predicted at $0.6 < X/C < 1.2$, which indicates that the separation bubble thickness may be over-predicted. The similar discrepancy is observed in all the U-RANS simulation conducted by other researchers [55, 56]. Further increase of mesh size does not change results as shown by the mesh refinement in Fig. 8.

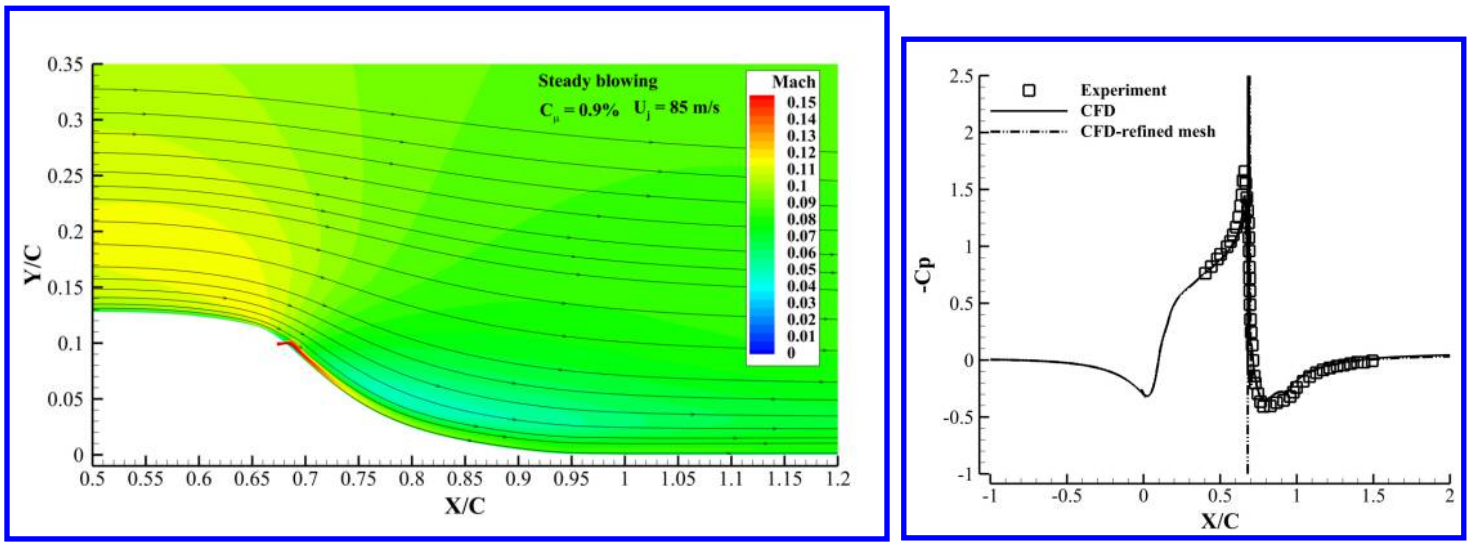

(a) Mach number contour (b) C_p distributions

Figure 7: CFD results of the hump with steady blowing

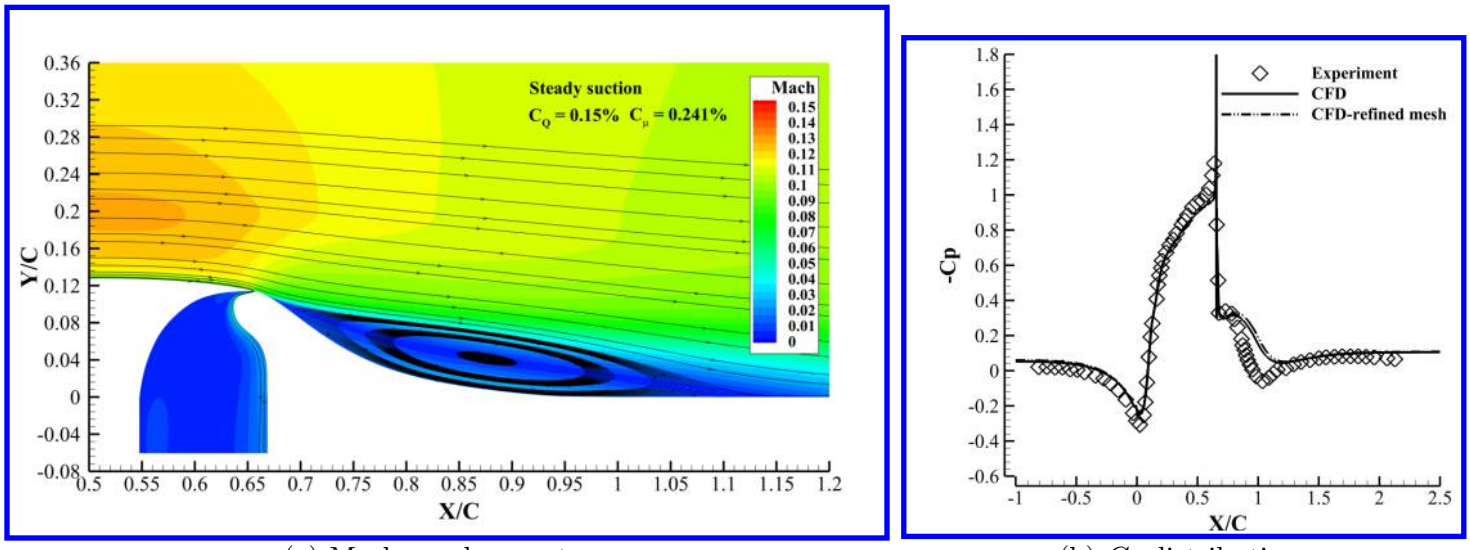

(a) Mach number contour (b) C_p distributions

Figure 8: CFD results of the hump with steady suction

4 Co-flow Jet Hump

As sketched in Fig. 9, the CFJ flow control is implemented by adding injection and suction slots at certain streamwise location on the original baseline hump surface [30]. For the CFJ hump, a small amount of mass flow is

drawn into the hump from downstream, pressurized and energized by a micro-compressor pumping system inside the hump, and ejected through the upstream injection slot tangential to the main flow. In the present simulation, the micro-compressor actuator is modeled by applying total pressure inlet BC at injection slot and static pressure outlet BC at suction slot. This treatment of the injection and suction is thoroughly validated in the previous work [43, 44, 45, 46, 47, 24, 48, 49, 50, 20, 51, 52].

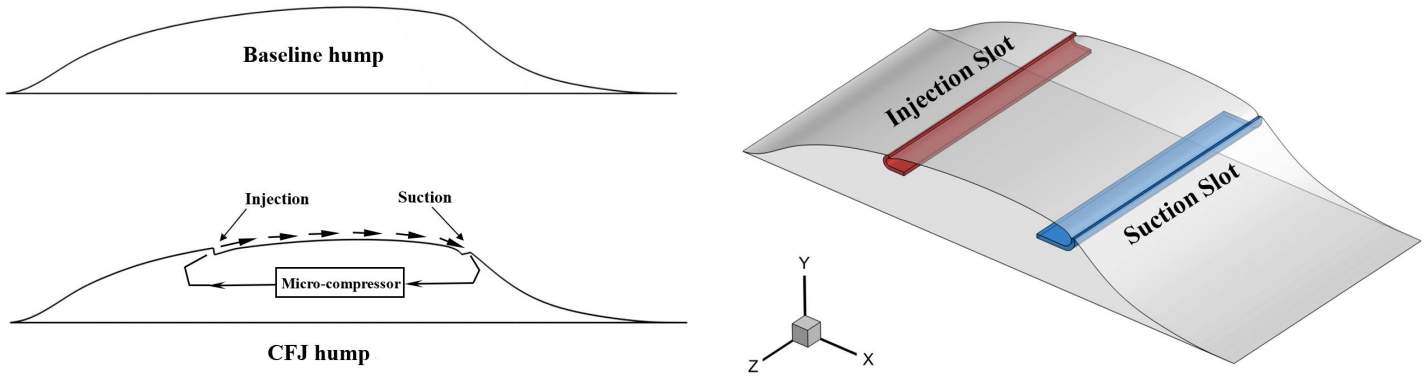

(a) 2D baseline hump and 2D CFJ hump

(b) 3D CFJ hump

Figure 9: Sketch of the CFJ hump

This section presents the trade studies of injection locations and suction locations. The objective is to find the optimum configuration to achieve fully removal of the flow separation with the minimum energy consumption.

4.1 Injection Location Study of CFJ Hump

As shown in Fig. 10, four injection locations are studied at 15%C, 30%C, 50%C and 67%C, which are measured from hump leading edge. For the injection locations at 15%C, 30%C and 50%C, the flow is ejected at positive slope of the hump, these cases are hence referred as positive slope injection (PSI). In all the PSI cases, suction location is fixed at 67%C with C_μ=0.011 and both the injection and suction slot size are 0.5%C (see Fig. 10 (a)). The flow ejected at 67%C as shown in Fig. 10 (b) is referred as the negative slope injection (NSI). In the NSI cases, suction location is fixed at 90%C with the injection slot size of 0.25%C and the suction slot size of 0.5%C. The C_μ is varied from 0.011 to 0.02.

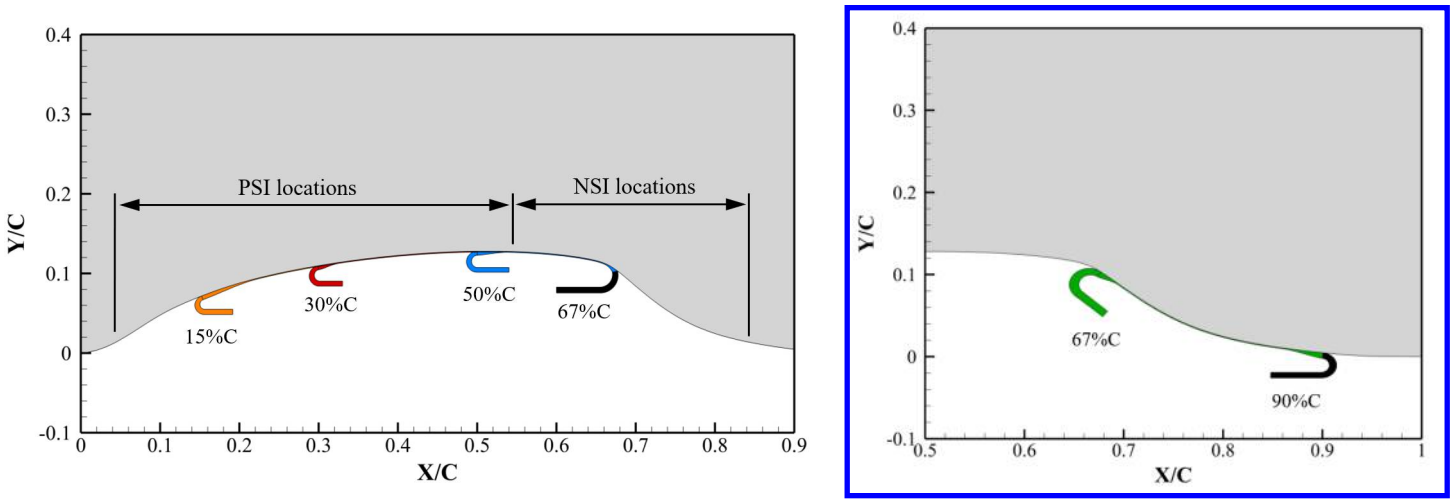

(a) PSI locations (b) NSI location

Figure 10: Illustration of injection locations

Fig. 11 (a) to (c) show the Mach number contours of the CFJ hump with PSI at injection location of 15%C, 30%C and 50%C. With C_μ=0.011, fully attached flow is achieved for all the PSI cases. In Fig. 11 (d) to (f), the Mach number contours of NSI cases are presented. A very small separation is observed at C_μ=0.011. When C_μ is increased to 0.015 and higher, the flow separation is completely removed.

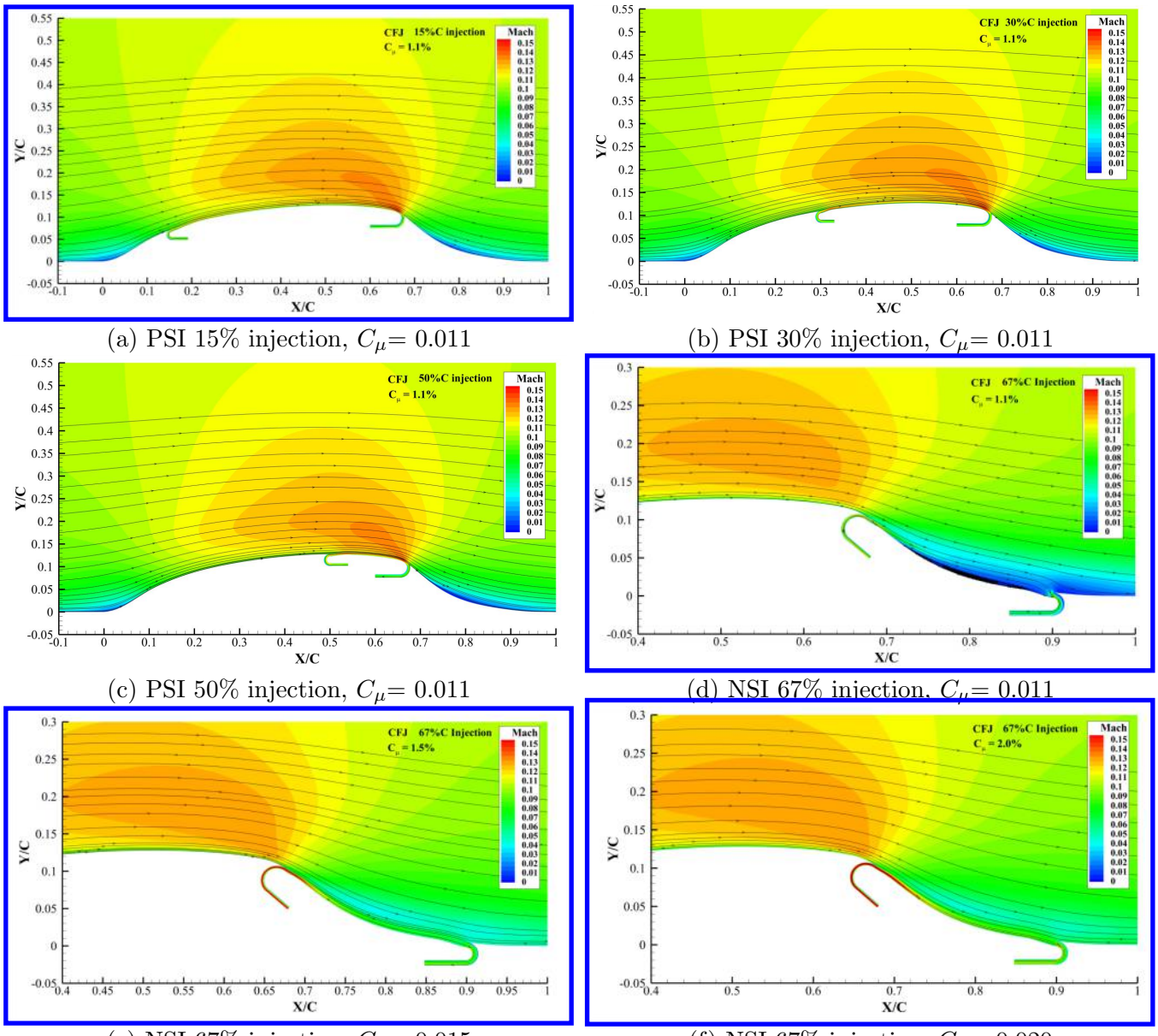

(a) PSI 15% injection, C_μ= 0.011

(b) PSI 30% injection, C_μ= 0.011

(c) PSI 50% injection, C_μ= 0.011

(d) NSI 67% injection, C_μ= 0.011

(e) NSI 67% injection, C_μ= 0.015

(f) NSI 67% injection, C_μ= 0.020

Figure 11: Mach number contours of injection location studies

The energy consumption is evaluated by two parameters: power coefficient defined by Eq. (2) and energy coefficient (C_E) defined by Eq. (4). C_E was introduced by Seifert et al. [57] and Woszidlo [58] for studies of fluidic oscillators. It assumes that static pressure is converted to dynamic pressure, in which total pressure are fully represented by kinematic energy.

$$C_E = \frac{P}{\frac{1}{2}A_{ref}\rho_\infty {U_\infty}^3} = \frac{(\frac{1}{2}\rho_{jet}{U_{jet}}^2)A_{nozzle}U_{jet}}{\frac{1}{2}A_{ref}\rho_\infty {U_\infty}^3} = \frac{C_\mu}{2} \bullet \frac{U_{jet}}{U_\infty} \tag{4}$$

where A_{nozzle} is the total area of discrete injection nozzles; U_j is the jet velocity.

Since C_E is used by other researchers [57, 58], both C_E and P_c are used in this paper to evaluate the power consumption. For injection or suction only flow control, since there is no information for flow withdrawing or discharging, the P_c is not calculated. Only C_E is evaluated.

Table 1 compares the flow separation control and the energy consumption of various injection location cases. As injection location moves from 15%C to 50%C, the C_E remains constant, but the P_c gradually decreases and reaches minimum at 50%C. This is because the suction peak of baseline hump locates at about 50%C as shown in Fig. 6 (b). Ejecting the flow near the suction peak with the lowest pressure requires the least power. The case with the injection right upstream of the separation bubble at 67%C requires higher C_μ, C_E, and P_C, because the static pressure at the injection location is high and hence more energy is needed to eject the flow. This is an important principle of active flow control, which indicates that the required power is linearly determined by the jet mass flow rate, but exponentially determined by the pressure ratio [33]. In other words, using higher mass flow rate and lower pressure ratio is more energy efficient.

Table 1: Power consumption of injection location studies cases

Cases	Inj location	Suc location	C_μ	U_{jet}/U_∞	C_E	P_C	Flow
CFJ 1	15%C	67%C	0.011	1.05	0.0058	0.0075	Fully attached
CFJ 2	30%C	67%C	0.011	1.05	0.0058	0.0070	Fully attached
CFJ 3	50%C	67%C	0.011	1.05	0.0058	0.0053	Fully attached
CFJ 4	67%C	90%C	0.015	1.48	0.016	0.011	Fully attached

4.2 Suction Location Study of CFJ Hump

The suction location variations of co-flow jet AFC are studied in this section to obtain the optimum combination of injection and suction location for minimizing the energy consumption. Two injection locations are used for the suction location study. One is at 50%C with PSI and the other is at 67% with NSI. The 50%C is the minimum energy consumption location obtained in the injection location trade study. The 67%C injection location is the flow separation onset location of the baseline hump with no flow control. It is also at about the same location of the injection and suction only flow control used in the NASA hump study [31, 29]. For the PSI cases, suction locations of 70%C, 75%C, 80%C and 85%C are studied as shown in Fig. 12 (a). For the NSI cases, the suction location is at 75%C, 80%C and 85%C as shown in Fig. 12 (b). A slot-size of 0.5% is used for all the injection and suction slots.

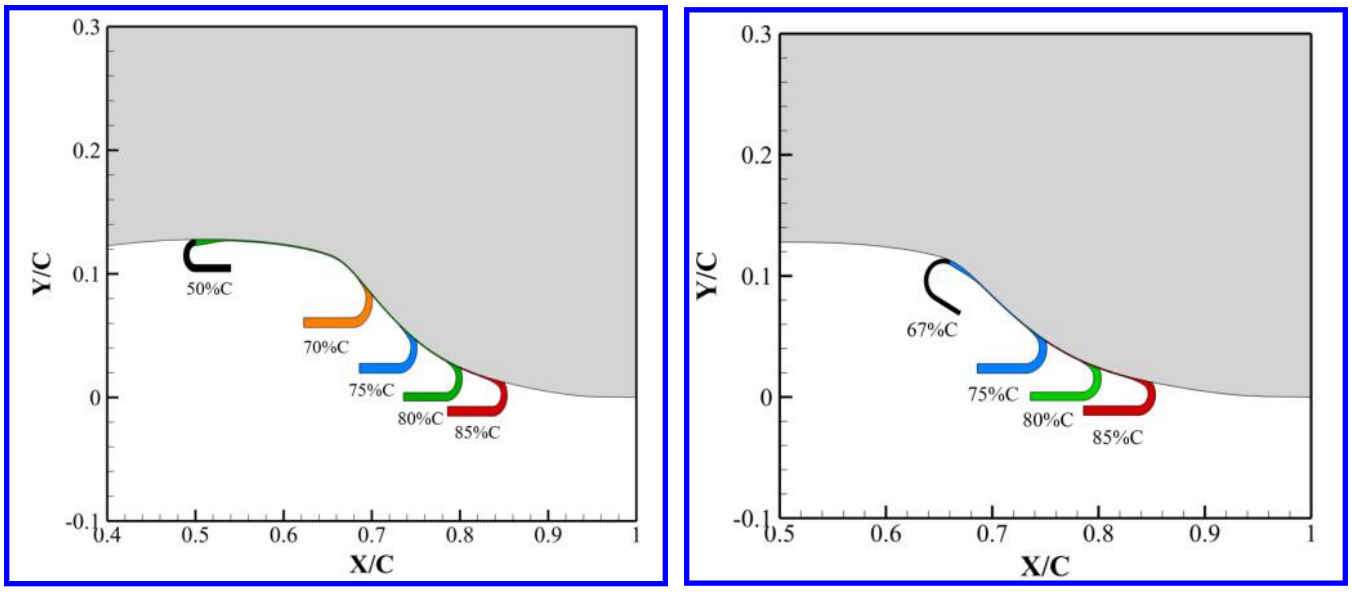

(a) Suction location studies for PSI (b) Suction location studies for NSI

Figure 12: Illustration of the CFJ hump with different suction locations

Fig. 13 shows the Mach number contours of various suction locations for the PSI cases. In PSI studies, C_μ of 0.015 is used to study the flow separation with the variation of suction locations. Flow reattachment is achieved at suction location of 70%C as shown in Fig 13 (a). As the suction location moves downstream to 75%C, 80%C and 85%C, the flow is gradually separated with C_μ kept at 0.015. The flow separation is minor for the suction location of 75%C, but grow larger at 80%C and 85%C. This phenomenon indicates that using CFJ with both injection and suction upstream of the severe APG area is more effective and efficient to energize the boundary layer and remove downstream flow separation. An attached boundary layer is more efficient for energy transfer by turbulent mixing between the jet and main flow. Putting the injection in the separation region is not so effective to remove the flow separation.

Suction location of 70%C has the lowest energy expenditure as shown in Fig. 13 (e), for which full flow attachment is achieved with a C_μ of 0.0077. It is observed that the 70%C reaches the minimum slope and is a deflection point. Fig. 15 shows the hump surface slope distribution in axial direction. The negative slope indicates the hump suction surface is diverging and creates a growing adverse pressure gradient (APG). In location 70%C, the hump slope reaches the minimum value of -0.85, which means the duct area reaches the fastest diverging rate and the flow has the maximum adverse pressure gradient at that location. Suction at such location appears to be the most effective to reduce the maximum APG and make the flow attached.

Mach contours of the NSI cases with various suction locations are shown in Fig. 13. With the injection located at 67%C, the separation onset point, C_μ of 0.012 is the minimum to remove the separation with the suction located at 75%C the flow remains attached with an extended low velocity region between the injection and suction when the suction is moved further downstream at 80%C and 85%C. C_μ of 0.012 is 56% larger than the minimum C_μ of 0.0077 required for the PSI case, which again indicates that placing the CFJ upstream of the flow separation region is more efficient than putting it in the flow separation region.

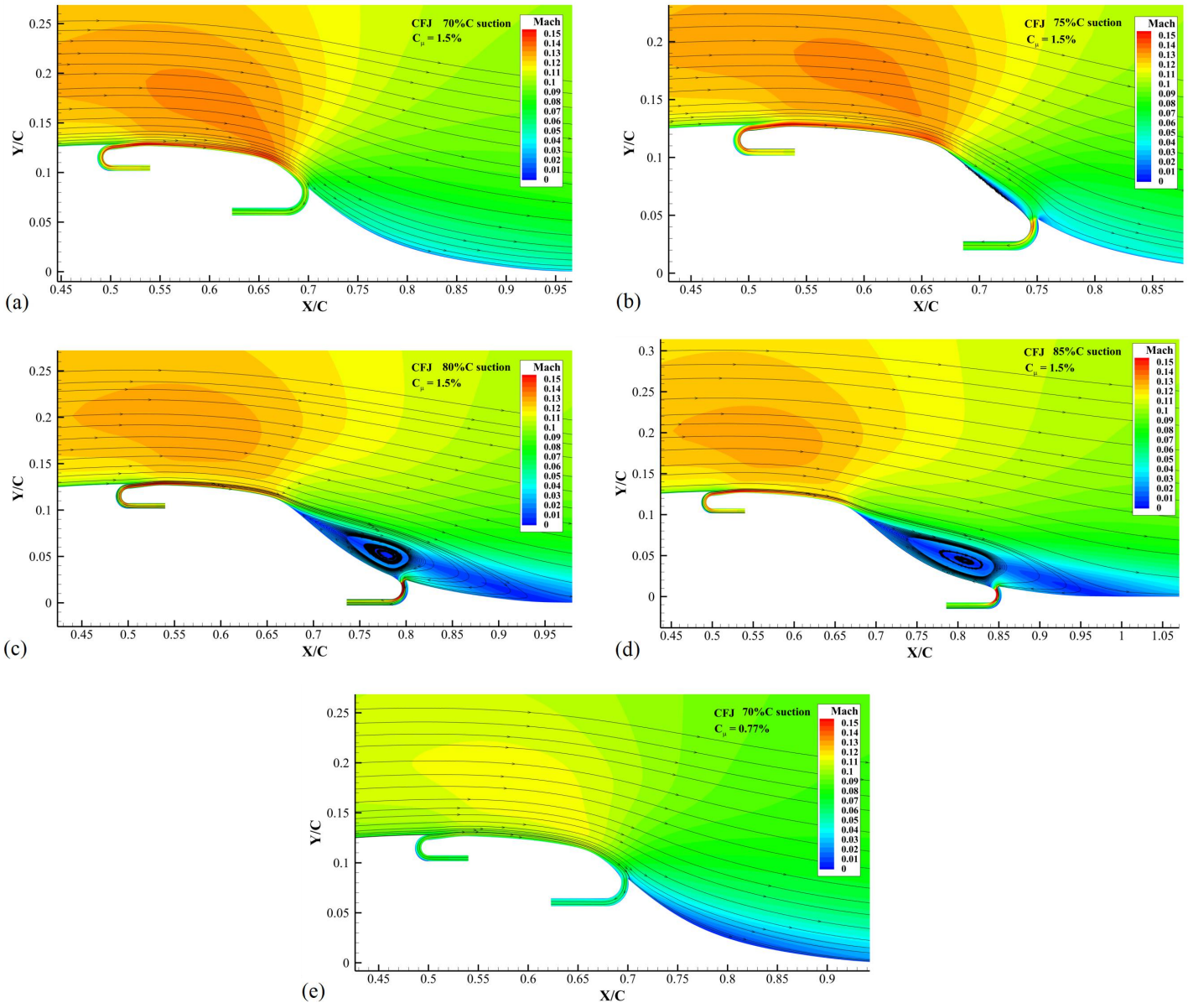

Figure 13: Mach number contours of PSI suction location studies: (a) 70%, C_μ= 0.015, (b) 75%, C_μ= 0.015, (c) 80%, C_μ= 0.015, (d) 85%, C_μ= 0.015, (e) 70%, C_μ= 0.0077.

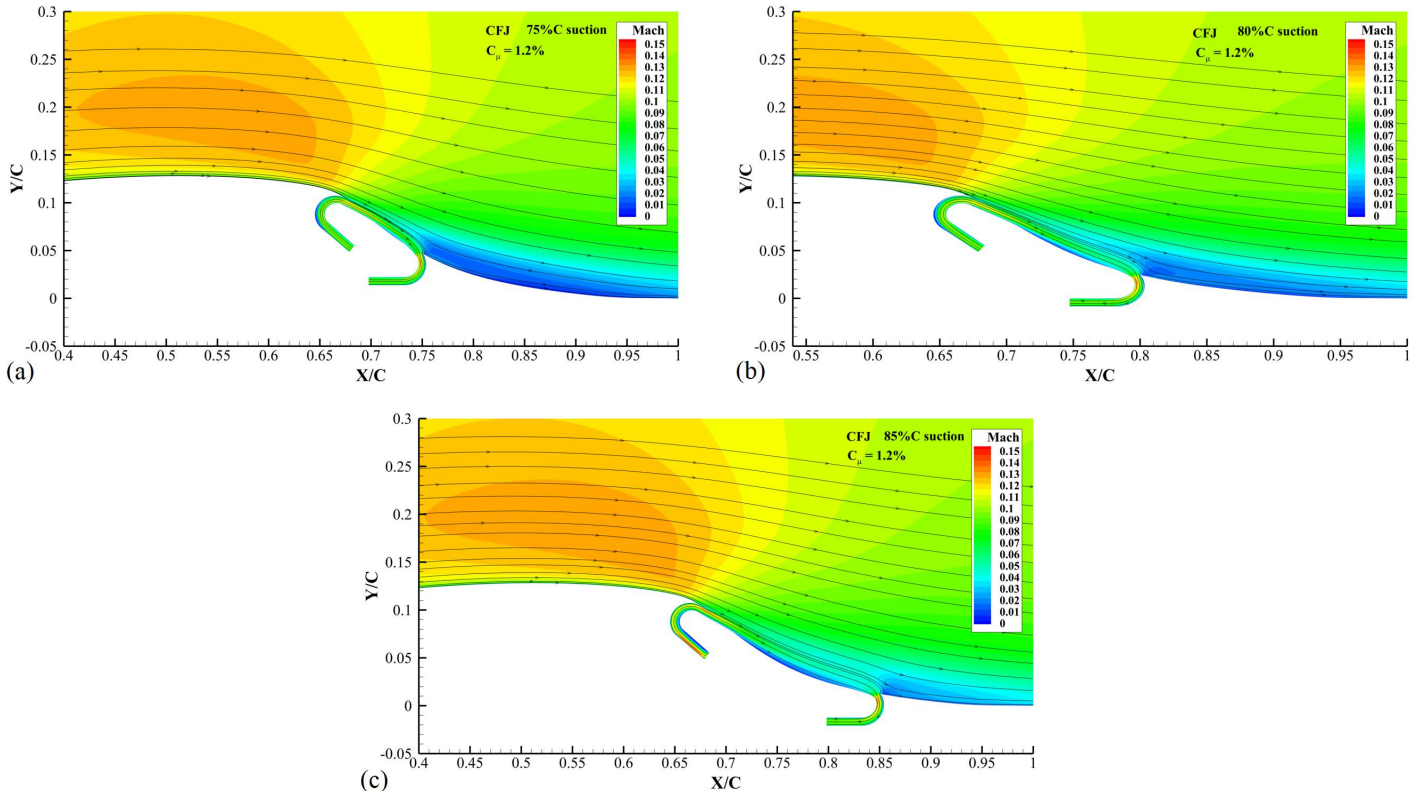

Figure 14: Mach number contours of NSI suction location studies: (a) 75%, C_μ= 0.012, (b) 80%, C_μ= 0.012, (c) 85%, C_μ= 0.012.

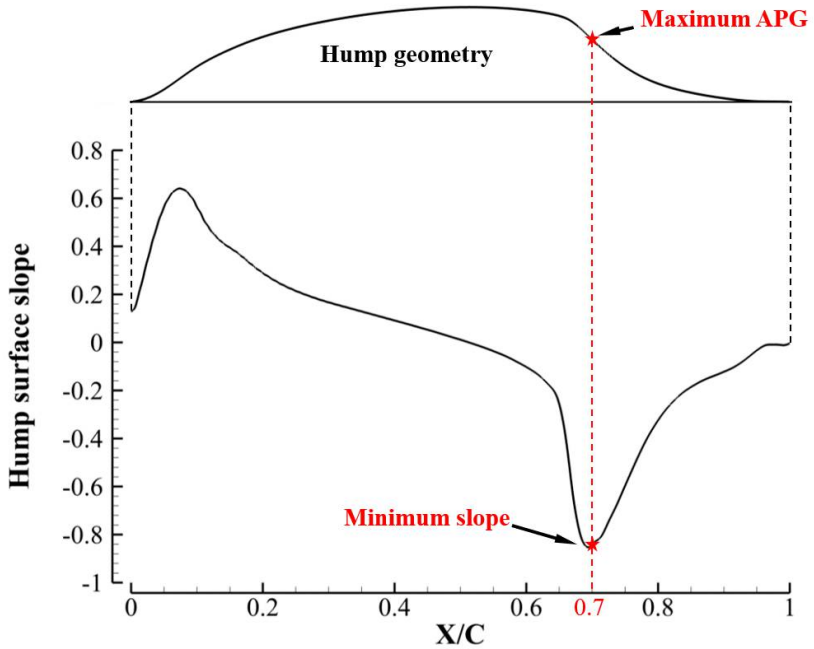

Figure 15: Distribution of hump surface slope

Fig. 16 compares the C_P distributions of the baseline NASA hump, the suction only flow control [29] with C_μ of 0.0073 and 0.026, and the optimum CFJ hump with injection at 50%C, suction at 70%C and C_μ of 0.0077. The steady suction flow control are tested in [29], where the data of the C_p and energy consumption for steady suction 1 are available and steady suction 2 only has C_p available.

For the CFJ hump, the suction peak C_p value of 1.5 is more than twice of the baseline one and the suction peak location is also moved from 50%C for the baseline to about 65%C, right before the suction slot location. This also means that the most efficient jet mixing with the main flow occurs under favorable pressure gradient. This is a new phenomenon that is not observed before since the CFJ mixing usually occurs under adverse pressure gradient. After the suction peak, the pressure rises sharply from 65%C to 70%C due to the rapid expansion of the duct area and the attached flow. Because of the more than doubled suction peak, the main flow momentum is substantially higher and is able to resist the sever adverse pressure gradient to keep the flow attached. For the suction only flow control, the steady suction 1 has the similar energy consumption with the presented CFJ cases but only partially removes flow separation as indicated by the flat region on the C_p plot. The steady suction 2 can fully attach the flow but with a significantly higher energy consumption as the C_μ is more than tripled.

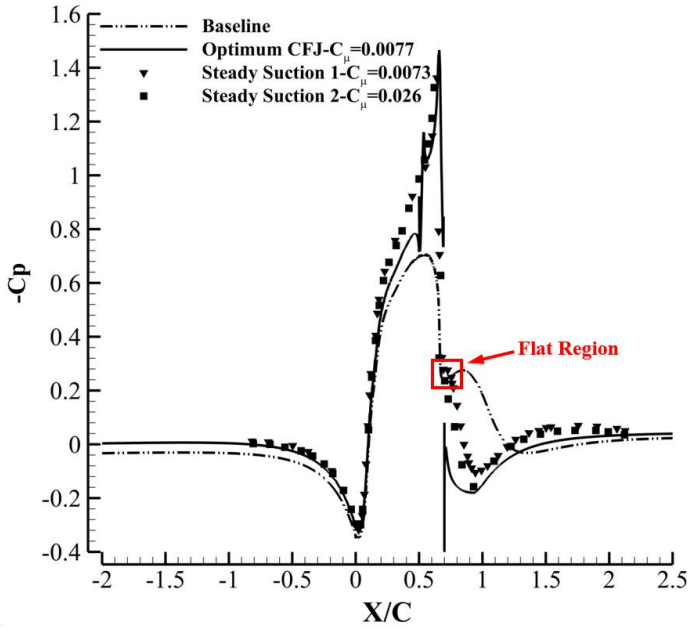

Figure 16: C_P distributions of optimum CFJ hump, baseline hump and the hump with steady suction

Table 2 presents the energy expenditure of C_E and P_c for all the CFJ suction location trade study cases with attached flow. For the PSI cases (CFJ 5-8), C_E and P_c gradually increases as suction location moves more downstream. For the NSI cases (CFJ 9-10), the C_E remains the same, but the P_c is reduced as suction moves from 75% to 85%. This is because that a more downstream suction position has a more diffused flow and a higher main flow pressure, which makes the suction easier with lower required power. The steady suction 1 has the same level of energy consumption with the presented CFJ cases, and is therefore used here for comparison. Note that the steady suction 1 can only partially attach the flow. Comparatively, a fully attached flow is achieved in the optimum CFJ case (CFJ 5) with a smaller C_E, which indicates the high effectiveness and energy efficiency of CFJ active flow control. Additionally, steady suction is not ZNMF, which means a higher energy consumption and system complexity should be considered than the present case.

Table 2: Power consumption of suction location cases

Cases	Inj location	Suc location	C_μ	U_{jet}/U_∞	C_E	P_C	Flow
CFJ 5	50%C	70%C	0.0077	0.88	0.0034	0.0032	Fully attached
CFJ 6	50%C	75%C	0.0175	1.32	0.012	0.011	Fully attached
CFJ 7	50%C	80%C	0.019	1.38	0.013	0.015	Fully attached
CFJ 8	50%C	85%C	0.022	1.49	0.016	0.016	Fully attached
CFJ 9	67%C	75%C	0.012	0.948	0.00569	0.0066	Fully attached
CFJ 10	67%C	80%C	0.012	0.943	0.00566	0.0048	Fully attached
CFJ 11	67%C	85%C	0.012	0.943	0.00566	0.043	Fully attached
Steady Suction 1	-	65%C	0.0073	1.38	0.005	-	Partially attached

5 More Comparison with the Injection Only

The purpose of this section is to compare the injection only flow control with the CFJ hump studied in Section 4.1 using the same injection location, orientation and slot size. The performance difference is thus only due to the existence of the suction slot of CFJ. The injection locations include 15%C, 30%C, 50%C and 67%C, among which the 50%C is the optimum injection location for CFJ and is at the suction peak location for the hump configuration.

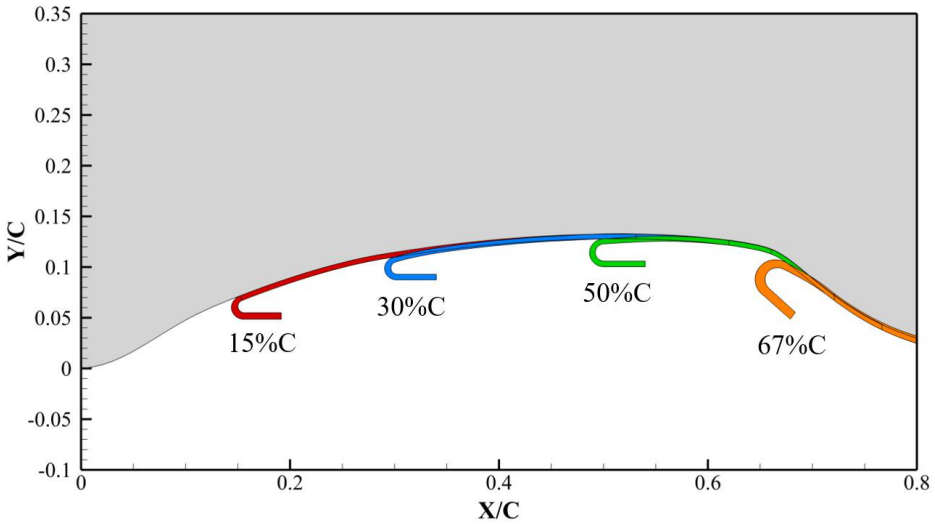

Figure 17: Illustration of injection locations

In Section 4.1, the CFJ with injection located at 15%C and 30%C fully removes the separation with C_μ of 1.1%. The Mach number contours in Fig. 18 (a) and (b) show that the flow is massively separated with the injection located at 15%C and 30%C at a more than twice higher C_μ of 2.5%. Without the downstream suction of the CFJ flow control, the main flow energy enhanced by the injection only is quickly dissipated and hardly alters the flow. When the injection location is located closer to the separation area at 50%C and 67%C, the injection only flow control is indeed more effective than the injection located more upstream.

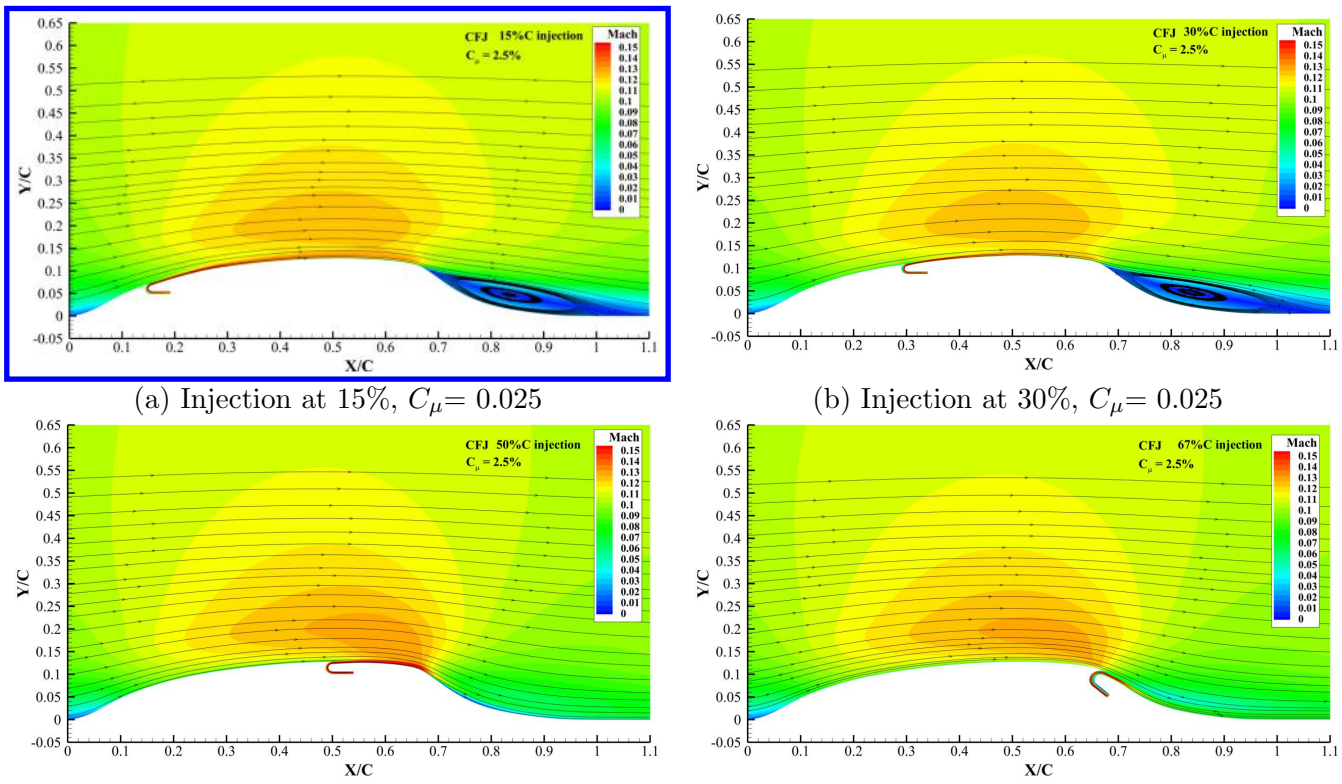

(a) Injection at 15%, C_μ= 0.025

(b) Injection at 30%, C_μ= 0.025

(c) Injection at 50%, C_μ= 0.025

(d) Injection at 67%, C_μ= 0.025

Figure 18: Mach number contours of injection only CFJ cases

Table 3 presents the minimum C_μ to achieve full attachment in each studied injection location, among which the case Inj Only 4 with the 67%C injection location has the lowest energy expenditure. This conclusion indicates that if an injection only flow control is used, it is indeed most effective to place the injection right at the separation onset location. This is different from the previous observation for CFJ flow control, which has the most efficient injection located at the suction peak location at the 50%C. By comparing the optimum injection only case (Inj Only 4) with the optimum CFJ case 5, the former has an energy coefficient C_E of 0.0055, which is 63% higher than that of the latter with C_E of 0.0034. This again numerically proves that the CFJ flow control with both injection and suction is much more efficient than the flow control with injection only. Furthermore, the injection only flow control has to solve the flow source problem to provide the jet mass flow. The CFJ flow control is a self-contained ZNMF flow control and has no issue to provide any amount of mass flow required.

Table 3: Power consumption of injection-only cases

Cases	Injection location	Suction location	C_μ	U_{jet}/U_∞	C_E	P_C	Flow
Inj Only 1	15%C	-	0.056	2.36	0.066	-	Fully attached
Inj Only 2	30%C	-	0.038	1.94	0.037	-	Fully attached
Inj Only 3	50%C	-	0.025	1.59	0.020	-	Fully attached
Inj Only 4	67%C	-	0.012	0.93	0.0055	-	Fully attached
Steady Suction 1	-	65%C	0.0073	1.38	0.005	-	Partially attached

6 Conclusions

This paper applies Co-flow Jet (CFJ) active flow control (AFC) on NASA hump and numerically studies its flow control performance to suppress flow separation at low energy expenditure. The effects of the CFJ injection and suction locations are studied. The experimental results of the baseline hump and the hump with steady blowing and suction are used to validate the accuracy of numerical method. The high fidelity in-house CFD code FASIP with the 2D Unsteady Reynolds averaged Navier-Stokes (URANS) equations with one-equation Spalart-Allmaras model is utilized. The validation is overall in very good agreement with the experiment for the baseline and steady blowing cases.

The numerical simulation indicates that using co-flow jet for the hump separation control is very effective and energy efficient. With injection location at 50%C and suction location at 70%C, a full flow attachment is achieved at C_μ=0.0077 with the CFJ power coefficient (P_c) of 0.0032 and the energy coefficient (C_E) of 0.0034. This is consistent with the previous observation for CFJ airfoil that placing the injection at the suction peak location minimizes the AFC energy cost. The present study also discovers that the optimum location for CFJ suction is at the location the hump surface slope reaches the minimum, which gives the lowest energy consumption. A study is also conducted to move the CFJ injection location downstream to the baseline flow separation onset position at 67%C and move the suction location into the adverse pressure gradient area. Such configuration significantly increases the energy consumption. The study indicates that applying the CFJ upstream of the flow separation with mixing under favorable pressure gradient is much more efficient than applying it at the baseline flow separation area under the adverse pressure gradient.

To further investigate the role of suction in the CFJ active flow control, the injection-only flow control is designed and numerically studied. Compared with the CFJ case, the minimum energy consumption for the injection only case with the separation removed is increased by 57% with C_E of 0.0055. For the injection only flow control, the injection location for the minimum energy consumption is not at the suction peak location of 50%C as for the CFJ, but at the onset of separation location of 67%C. These results indicate that the suction of the CFJ flow control is very beneficial for two reasons: 1) It energizes the boundary layer and makes the CFJ energy consumption significantly lower than the injection only flow control; 2) It provides the source of the mass flow for injection to make the CFJ self-contained zero-next-mass-flux flow control to avoid introducing mass flow from other source, which will incur extra energy consumption.

7 Acknowledgment

The authors would like to acknowledge the computing resource provided by the Center of Computational Sciences at the University of Miami.

Disclosure: Dr. GeCheng Zha is on the Board of Directors/Corporate Officer for Co-flow Jet and holds equity in Co-flow Jet. Dr. Zha is also the inventor of intellectual property licensed to Co-flow Jet.

References

[1] L. T.O.G.Prandtl, *Applied hydro-and aeromechanics (Dover Books on Aeronautical Engineering)*, vol. 2. Dover Publications, 1934.

[2] R. J. Englar, "Circulation Control for High Lift and Drag Generation on STOL Aircraft," *Journal of Aircraft*, vol. 12, pp. 457–463, 1975.

[3] L. N. Cattafesta III and M. Sheplak, "Actuators for active flow control," *Annu. Rev. Fluid Mech.*, vol. 43, no. 3, pp. 247–272, 2011.

[4] A. Glezer and M. Amitay, "Synthetic Jets," *Annual Review of Fluid Mechanics*, vol. 24, 2002.

[5] M. Jain, B. Puranik, and A. Agrawal, "A numerical investigation of effects of cavity and orifice parameters on the characteristics of a synthetic jet flow," *Sensors and Actuators A: Physical*, vol. 165, no. 2, pp. 351–366, 2011.

[6] H. Mu, Q. Yan, W. Wei, and P. E. Sullivan, "Synthetic jet performance for different axisymmetric cavities analyzed with three-dimensional lattice-boltzmann method," *AIAA Journal*, vol. 56, no. 6, pp. 2499–2505, 2018.

[7] R. B. Kotapati, R. Mittal, and L. N. Cattafesta Iii, "Numerical study of a transitional synthetic jet in quiescent external flow," *Journal of Fluid Mechanics*, vol. 581, pp. 287–321, 2007.

[8] D. Greenblatt, K. B. Paschal, Y. Chung-Sheng, and J. Harris, "Experimental investigation of separation control part 2: zero mass-flux oscillatory blowing," *AIAA journal*, vol. 44, no. 12, pp. 2831–2845, 2006.

[9] Thomas, F., Kozlov, A. and Corke, T. C., " Plasama Actuators for Cylinder Flow Control and Noise Reduction," *AIAA Journal* , vol. 46, pp. 1921–1931, 2008.

[10] Z. Zhang, Y. Wu, M. Jia, H. Song, Z. Sun, H. Zong, and Y. Li, "The multichannel discharge plasma synthetic jet actuator," *Sensors and Actuators A: Physical*, vol. 253, pp. 112–117, 2017.

[11] C. Enloe, R. Mangina, and G. Font, "Normalized electronegative species effects in the dielectric-barrier-discharge plasma actuator," *AIAA Journal*, vol. 54, no. 7, pp. 2061–2068, 2016.

[12] L. Shen and C.-y. Wen, "Leading edge vortex control on a delta wing with dielectric barrier discharge plasma actuators," *Applied Physics Letters*, vol. 110, no. 25, p. 251904, 2017.

[13] P. Sujar-Garrido, N. Benard, E. Moreau, and J. Bonnet, "Dielectric barrier discharge plasma actuator to control turbulent flow downstream of a backward-facing step," *Experiments in Fluids*, vol. 56, no. 4, p. 70, 2015.

[14] W. Crowther and L. Gomes, "An evaluation of the mass and power scaling of synthetic jet actuator flow control technology for civil transport aircraft applications," *Proceedings of the Institution of Mechanical Engineers, Part I: Journal of Systems and Control Engineering*, vol. 222, no. 5, pp. 357–372, 2008.

[15] P. Gil and P. Strzelczyk, "Performance and efficiency of loudspeaker driven synthetic jet actuator," *Experimental Thermal and Fluid Science*, vol. 76, pp. 163–174, 2016.

[16] Z. Trávníček and J. Kordík, "Energetic efficiencies of synthetic jet actuators: Commentary on the article by gil and strzelczyk," *Experimental Thermal and Fluid Science*, vol. 98, pp. 121–123, 2018.

[17] J. Zito, D. Arnold, T. Houba, J. Soni, R. Durscher, and S. Roy, "Microscale dielectric barrier discharge plasma actuators: Performance characterization and numerical comparison." AIAA Paper 2012-3091, 43rd AIAA Plasmadynamics and Lasers Conference, New Orleans, Louisiana, June, 2012.

[18] Zha, G.-C and Paxton, C. and Conley, A. and Wells, A. and Carroll, B., "Effect of Injection Slot Size on High Performance Co-Flow Jet Airfoil," *AIAA Journal of Aircraft*, vol. 43, 2006.

[19] Zha, G.-C and Carroll, B. and Paxton, C. and Conley, A. and Wells, A., "High Performance Airfoil with Co-Flow Jet Flow Control," *AIAA Journal*, vol. 45, 2007.

[20] Lefebvre, A. and Dano, B. and Bartow, W. and Di Franzo, M. and Zha, G.-C., "Performance and Energy Expenditure of Co-Flow Jet Airfoil with Variation of Mach Number," *AIAA Journal of Aircraft*, vol. 53, pp. 1757–1767, 2016.

[21] Yang, Y.-C. and Zha, G.-C., "Super-Lift Coefficient of Active Flow Control Airfoil: What Is the Limit?." AIAA Paper 2017-1693, AIAA SCITECH2017, 55th AIAA Aerospace Science Meeting, Grapevine, Texas, 9-13 January 2017.

[22] G.-C. Zha, Y.-C. Yang, Y. Ren, and B. McBreen, "Super-lift and thrusting airfoil of coflow jet-actuated by micro-compressors." AIAA Paper 2017-3061, AIAA AVIATION 2018, Atlanta, GA , 25 - 29 June 2018.

[23] Zha, G.-C. and Gao, W. and Paxton, C., "Jet Effects on Co-Flow Jet Airfoil Performance," *AIAA Journal, No. 6,*, vol. 45, pp. 1222–1231, 2007.

[24] Wang, B.-Y. and Haddoukessouni, B. and Levy, J. and Zha, G.-C., "Numerical Investigations of Injection Slot Size Effect on the Performance of Co-Flow Jet Airfoil ," *AIAA Journal of Aircraft*, vol. 45, pp. 2084–2091, 2008.

[25] K. Xu and G. Zha, "Design of high specific speed mixed flow micro-compressor for co-flow jet actuators." GT2019-90980, Submitted to IGTI Turbo Expo 2019, Phoenix, Arizona, USA, June 17 - 21, 2019.

[26] J. Zhang, K. Xu, Y. Yang, Y. Ren, P. Patel, and G. Zha, "Aircraft control surfaces using co-flow jet active flow control airfoil." AIAA Paper 2018-3067, 2018 Applied Aerodynamics Conference, Atlanta, Georgia, June 25-29, 2018.

[27] K. Xu, J. Zhang, and G. Zha, "Drag minimization of co-flow jet control surfaces at cruise conditions." AIAA 2019-1848, AIAA Scitech 2019 Forum, San Diego, California, 7-11 January 2019.

[28] K. Xu and G. Zha, "High control authority 3d aircraft control surfaces using co-flow jet." AIAA 2019-3168, AIAA Aviation 2019, Dallas, Texas, 17-21 June 2019.

[29] C. Rumsey, "2dwmh: 2d nasa wall-mounted hump separated flow validation case." Turbulence Modeling Resource, turbmodels.larc.nasa.gov, 2003.

[30] D. Greenblatt, K. B. Paschal, C. S. Yao, J. Harris, N. W. Schaeffler, and A. E. Washburn, "Experimental investigation of separation control part 1: baseline and steady suction," *AIAA journal*, vol. 44, no. 12, pp. 2820–2830, 2006.

[31] D. Borgmann, A. Pande, J. Little, and R. Woszidlo, "Experimental study of discrete jet forcing for flow separation control on a wall mounted hump." AIAA Paper 2017-1450, AIAA SciTech 2017, 55th AIAA Aerospace Sciences Meeting, Grapevine, Texas, January 2017.

[32] Y. Wang and G.-C. Zha, "Study of 3D Co-flow Jet Wing Induced Drag and Power Consumption at Cruise Conditions." AIAA Paper 2019-0034, AIAA SciTech 2019, San Diego, CA, January 7-11, 2019.

[33] Y. Wang and G.-C. Zha, "Study of Super-Lift Coefficient of Co-Flow Jet Airfoil and Its Power Consumption." Submitted to AIAA Aviation 2019, AIAA Applied Aerodynamics Conference, Dallas, Texas, 17-21 June 2019.

[34] P. Spalart and S. Allmaras, "A One-equation Turbulence Model for Aerodynamic Flows." AIAA-92-0439, 30th Aerospace Sciences Meeting and Exhibit, Reno,NV,U.S.A., 06 January 1992 - 09 January 1992.

[35] Shen, Y.-Q. and Zha, G.-C., " Improved Seventh-Order WENO Scheme ." AIAA Paper 2010-1451, 48th AIAA Aerospace Sciences Meeting, Orlando, FL, Jan. 4-6, 2010.

[36] G.-C. Zha, Y. Shen, and B. Wang, "An improved low diffusion E-CUSP upwind scheme ," *Journal of Computer & Fluids*, vol. 48, pp. 214–220, 2011.

[37] Y.-Q. Shen, G.-C. Zha, and B.-Y. Wang, "Improvement of Stability and Accuracy of Implicit WENO Scheme ," *AIAA Journal*, vol. 47, pp. 331–344, 2009.

[38] Shen, Y.-Q. and Zha, G.-C. and Chen, X.-Y., " High Order Conservative Differencing for Viscous Terms and the Application to Vortex-Induced Vibration Flows," *Journal of Computational Physics*, vol. 228(2), pp. 8283–8300, 2009.

[39] Shen, Y.-Q. and Zha, G.-C. , " Improvement of the WENO Scheme Smoothness Estimator," *International Journal for Numerical Methods in Fluids*, vol. 64, p. DOI:10.1002/fld.2186, 2010.

[40] G.-C. Zha and E. Bilgen, "Numerical study of three-dimensional flows using unfactored upwind-relaxation sweeping algorithm," *Journal of Computational Physics*, vol. 125, no. 2, pp. 425–433, 1996.

[41] B.-Y. Wang and G.-C. Zha, "A General Sub-Domain Boundary Mapping Procedure For Structured Grid CFD Parallel Computation," *AIAA Journal of Aerospace Computing, Information, and Communication*, vol. 5, No.11, pp. 2084–2091, 2008.

[42] X.-Y. Chen and G.-C. Zha, "Fully coupled fluid–structural interactions using an efficient high resolution upwind scheme," *Journal of Fluids and Structures*, vol. 20, no. 8, pp. 1105–1125, 2005.

[43] G.-C. Zha, B. F Carroll, C. D. Paxton, C. A. Conley, and A. Wells, "High-performance airfoil using coflow jet flow control," *AIAA journal*, vol. 45, no. 8, pp. 2087–2090, 2007.

[44] A. Lefebvre, B. Dano, W. Bartow, M. Fronzo, and G. Zha, "Performance and energy expenditure of coflow jet airfoil with variation of mach number," *Journal of Aircraft*, vol. 53, no. 6, pp. 1757–1767, 2016.

[45] G. Zha, W. Gao, and C.D. Paxton, "Jet Effects on Co-Flow Jet Airfoil Performance," *AIAA Journal*, vol. 45, pp. 1222–1231, 2007.

[46] G.-C. Zha, C. Paxton, A. Conley, A. Wells, nd B. Carroll, "Effect of Injection Slot Size on High Performance Co-Flow Jet Airfoil," *AIAA Journal of Aircraft*, vol. 43, pp. 987–995, 2006.

[47] Yang, Yunchao and Zha, Gecheng, "Super-Lift Coefficient of Active Flow Control Airfoil: What is the Limit?," *AIAA Paper 2017-1693, AIAA SCITECH2017, 55th AIAA Aerospace Science Meeting, Grapevine, Texas*, p. 1693, 9-13 January 2017.

[48] B. P. E. Dano, D. Kirk, and G.-C. Zha, "Experimental Investigation of Jet Mixing Mechanism of Co- Flow Jet Airfoil." AIAA-2010-4421, 5th AIAA Flow Control Conference, Chicago, IL, 28 Jun - 1 Jul 2010.

[49] B. P. E. Dano, G.-C. Zha, and M. Castillo, "Experimental Study of Co-Flow Jet Airfoil Performance Enhancement Using Micro Discreet Jets." AIAA Paper 2011-0941, 49th AIAA Aerospace Sciences Meeting, Orlando, FL,, 4-7 January 2011.

[50] Lefebvre, A. and Zha, G.-C. , "Design of High Wing Loading Compact Electric Airplane Utilizing Co-Flow Jet Flow Control." AIAA Paper 2015-0772, AIAA SciTech2015: 53nd Aerospace Sciences Meeting, Kissimmee, FL, 5-9 Jan 2015.

[51] Liu, Z.-X. and Zha, G.-C., "Transonic Airfoil Performance Enhancement Using Co-Flow Jet Active Flow Control." AIAA Paper 2016-3066, AIAA Aviation, June 13-17 2016.

[52] Lefebvre, A. and Zha, G.-C., "Trade Study of 3D Co-Flow Jet Wing for Cruise Performance." AIAA Paper 2016-0570, AIAA SCITECH2016, AIAA Aerospace Science Meeting, San Diego, CA, 4-8 January 2016.

[53] K. Kara, D. Kim, and P. J. Morris, "Flow-separation control using sweeping jet actuator," *AIAA journal*, vol. 56, no. 11, pp. 4604–4613, 2018.

[54] P. Poisson-Quinton and L. Lepage, "Survey of french research on the control of boundary layer and circulation," *Lachmann, GV,Boundary layer and Flow Control. Its Principles and Application*, vol. 1, pp. 21–73, 1961.

[55] F. Capizzano, P. Catalano, C. Marongiu, and P. L. Vitagliano, "U-RANS modelling of turbulent flows controlled by synthetic jets." AIAA Paper 2005-5015, 35th AIAA Fluid Dynamics Conference and Exhibit,Toronto, Ontario, Canada, 06 June 2005 - 09 June 2005.

[56] D. You, M. Wang, and P. Moin, "Large-eddy simulation of flow over a wall-mounted hump with separation control," *AIAA journal*, vol. 44, no. 11, pp. 2571–2577, 2006.

[57] A. Seifert, S. Eliahu, D. Greenblatt, and I. Wygnanski, "Use of piezoelectric actuators for airfoil separation control," *AIAA journal*, vol. 36, no. 8, pp. 1535–1537, 1998.

[58] R. Woszidlo and I. Wygnanski, "Parameters governing separation control with sweeping jet actuators." AIAA Paper 2011-3172, 29th AIAA Applied Aerodynamics Conference, Honolulu, Hawaii, 27 June 2011 - 30 June 2011.